Ground Reflection Interaction with Height-of-Burst Metalized Explosions

R. C. Ripley[1], L. Donahue[1], T. E. Dunabr[1], S. B. Murray[2], C. J. Anderson[2], F. Zhang[2], and D. V. Ritzel[3]

[1] *Martec Limited, 1888 Brunswick Street, Suite 400, Halifax, Nova Scotia, B3J 3J8, Canada*
[2] *DRDC Suffield, P.O. Box 4000, Station Main, Medicine Hat, Alberta T1A 8K6, Canada*
[3] *Dyn-FX Consulting Limited, 19 Laird Avenue N., Amherstburg, Ontario N9V 2T5, Canada*

Summary. Near-field impulse from metalized explosives is dominated by afterburning energy release and is influenced by a small confinement effect that is caused by ground reflected shock in height-of-burst (HOB) scenarios. The ground reflected shock interacts with the fireball, reheating the detonation products and distorting the fireball interface which promotes afterburning chemistry. The air behind the primary reflected shock is doubly shock heated which improves the local heating rate of the dispersed metal particles to their ignition temperature. Shock reverberation between the ground and expanding fireball, interaction with the emerging secondary shock, arrival of incident particle front and localized enhanced chemistry have a compounding effect and lead to increased loading observed on the ground. These effects are of particular interest for structural response resulting from near-field explosions.

1 Height-of-Burst Scenarios

The experimental configuration for the height-of-burst scenario (shown schematically in Figure 1), including diagnostic locations and mixture formulations is described in the companion paper by Murray et al. [1]. Two in-service weapons-grade thermobaric explosive (TBX) mixtures and two high-metal content improvised explosive formulations (IEF) were modeled and compared to experiment as well as high-explosive C4 (91% RDX) reference charges. Nominal 20-kg spherical charges cased in thin polyethylene at 3 m HOB are the focus of this paper. All metalized explosives have a nominal 10% C4 booster by mass. Since the explosive mass and compositions vary in addition to the particle morphology and metal content, direct comparison was not always possible, however phenomenology is discussed. Numerical predictions were compared with high-quality experimental data to augment experimental observations and help elucidate flow physics.

2 Numerical Explosion Afterburning Model

Numerical modeling of metalized explosives remains a challenge in the simulation community due to the dense chemically-reacting multiphase flow, with the degree of confinement increasing complexity of the simulations. Although even the best models may need to be adjusted based on experimental data, they offer additional insight into the flow field beyond the capability of experimental diagnostics, such as the evolution of afterburning reactivity and the internal temperature distribution. Unlike simple afterburning models (e.g., see [5, 6]), the present work employs full chemically reacting multiphase flow models. Details of the model are given in Ripley et al. [7].
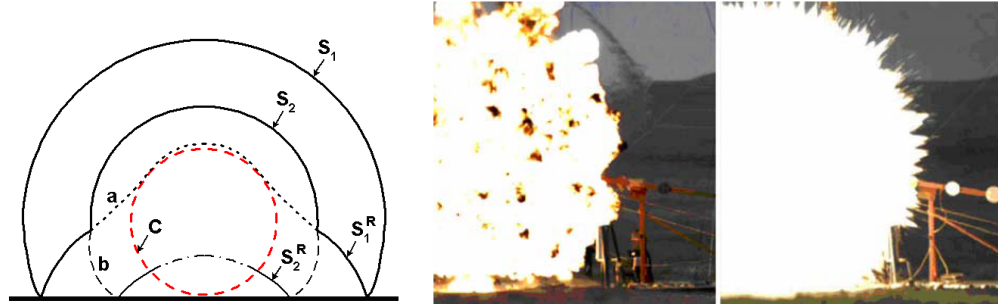
Fig. 1. Illustration of height-of-burst scenario (left to right: schematic, C4 trial, IEF1 trial). Figure nomenclature: S_1, incident primary shock; S_2, incident secondary shock; S_1^R, reflected primary shock; S_2^R, reflected secondary shock; C, contact surface (fireball); a, acceleration of ground reflected wave through shock-heated zone and fireball; and, b, acceleration of secondary shock through double-shock-heated zone.

The Chinook code is a parallel 3D unstructured mesh CFD code for simulation of time-accurate explosion events. It was developed by Martec and DRDC and used to model the experiments. The multiphase fluid-dynamic equations governing the flow include conservation of mass, momentum, energy, material concentrations, and particle number density. The Chinook code features a second-order HLLC approximate Riemann solver for both the fluid and particle phases, each of which has independent velocity and temperature fields. Gas-particle interactions are simulated using phase exchange source terms, which are based on empirical correlations for drag, convective heat transfer and mass transfer (metal particle combustion).

Equations of state for each material close the system of equations including: shock-Hugoniot EOS for condensed reactants; JWL for gaseous detonation products with explosive fitting parameters calculated using Cheetah; ideal gas law for surrounding atmosphere and air-blast; and, a phenomenological EOS for solid particles. High resolution meshes are used to resolve the details of the initiation region (size and location), booster configuration, charge shape, detonation wave propagation through the heterogeneous mixture, expansion and afterburning of gaseous detonation products (fireball), transmission of the blast wave into ambient air, and dispersal, heating and afterburning of metal particle additives with oxidizing gas species.

Detonation of the condensed explosive (powdered explosive, solid oxidizer granules and/or liquid monopropellant) is modeled using a global Arrhenius reaction rate. Detonation product gas species from the booster and bulk explosive are modeled using Cheetah chemical equilibrium for the CJ state. Gas-phase afterburning reactions are simulated for C, CO, H_2 and C_2H_2 with O_2 from the surrounding air. Metal particle reaction with O_2, CO, CO_2, and H_2O oxidising gas species are computed according to a diffusion-limited d^2 rate law.

3 Near-field TBX Phenomena

Free field and HOB fundamental TBX physics are covered in detail in the companion paper by Ritzel et al. [2]. These are: delayed incident time of arrival (TOA), lower primary peak overpressure in near field, noisy shock front due to particle and fireball jetting,

advanced secondary shock that diminishes negative phase and increases positive-phase impulse.

3.1 Fireball Interaction

In general, the TBX fireball size is larger than for HE and occurs later in time. For the C4 reference charge, the maximum fireball radius was 2.41 m, while the IEF fireball radius surpassed that of the C4 and is still expanding after 4.0 ms when the reflected primary shock returns and alters the fireball flow field. In the case of the C4 reference explosive, the detonation products are cold ($\approx$ 500 K) except at the fireball-air interface where detonation products afterburning occurs. The IEF fireball is hot due to late-time afterburning of the detonation products and metal particles which accelerates the ground reflection through the fireball. The cold booster gasses are visible at the initial HOB location. The IEF maximum fireball expansion is larger, the fireball is less dense, and it expands at a higher velocity. Large size is exaggerated in experimental video due to particle reaction outside the detonation products. The Rayleigh-Taylor instability is less prominent in the IEF explosion due to the smaller density discontinuity, owing to the hot detonation products, and diffusive effects as the particles cross the contact interface. This is consistent with the simple afterburning results presented in [4]. Measurement of the fireball speed showed that initially the C4 fireball was expanding faster within the first 1.2 ms, after which the IEF1 fireball expands faster (traveling up to 10% faster at 2 ms). This is significant as it translates into a piston effect that the target observes as impulse.
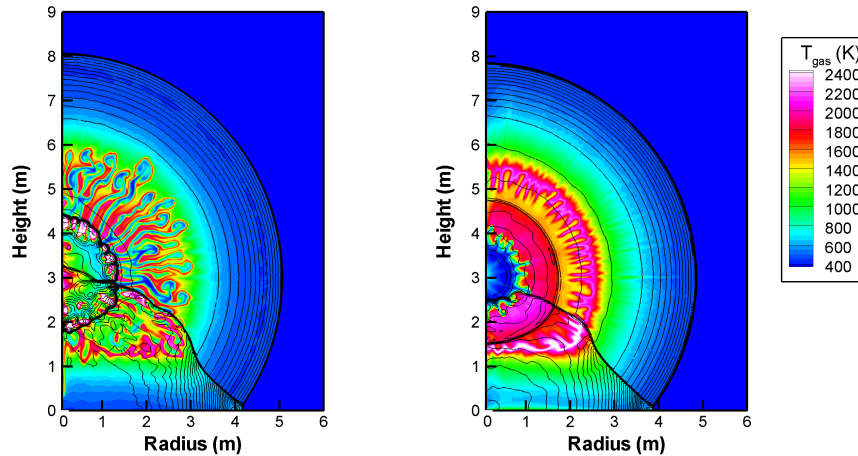
Fig. 2. Comparison of flow-field temperature distribution at 4 ms using 5-mm resolution mesh. C4 reference explosive (left) and IEF1 (right).

3.2 Incident Shock Reflection

Figure 3 illustrates the experimental and numerical results at gauge P2 (located on ground at 1.375 m radius). The ground reflection gauge history illustrates the explosive

characteristics and relative performance of the formulations (note that the actual charge masses vary from 18.5 kg to 21.3 kg). Delayed time of arrival (TOA) and weaker primary front are due to reduced explosive fraction of charge mass and momentum transfer required as the detonation accelerates metal particles. The TOA is 1.81 ms for C4, 1.83 ms for TBX1, 1.69 ms for TBX2, 2.05 ms for IEF1 and 1.80 for IEF2. The TBX formulations feature high VOD explosives with small metal flake that reacts promptly in the detonation products.
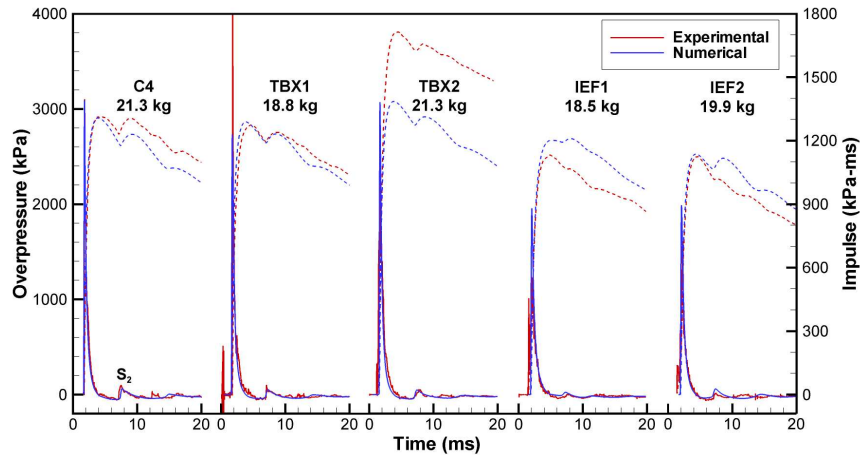
Fig. 3. Comparison of ground reflection results (Gauge P2). Pressure in solid lines; Impulse in broken lines.

3.3 Secondary Shock

Gauge P2 shown in Figure 3 clearly shows the magnitude and TOA of the secondary shock (S2) which forms as the collapse of the out-swept expansion shock that must travel through the detonation products, fireball interface, dispersed particle cloud and upwards-traveling ground-reflected shock. Accurate modeling of the secondary shock is therefore dependent on correct equations of state, afterburning reactions and explosive modeling parameters. Advancement of secondary shock increases impulse by diminishing the negative phase in both TBX and IEF. The secondary shock forms at 2.65 ms for IEF1 compared to 2.95 ms for C4. Figure 3 demonstrates good agreement in both primary and secondary shock arrival times indicating correct physical and numerical models.

4 Multiphase Explosion Flow Field

Even simple models [5, 6] can demonstrate non-ideal waveforms in the free field, however near field and semi-confined explosion situations require multiphase fluid dynamic solutions [7] to capture the thermochemical behaviour. Prediction of peak impulse depends on the positive phase of the pressure history and is particularly sensitive to the secondary shock arrival time. Detonation products afterburning and metal particle combustion significantly affect the gas flow-field temperature and density, thereby influencing

the secondary shock speed. Afterburning is dependent on flow-field temperature, mixing and spatial distribution of fuels and oxidizers. In the HOB scenario, the ground-reflected shock influences both the distribution and temperature of the reacting flow field.

Approximately 0.5 ms after the incident shock arrival, the ground reflected shock interacts with the expanding fireball. For IEF1, the particle front reaches the ground ahead of the incident primary shock. Figure 4 illustrates the spatial distribution of particles relative to the IEF1 fireball. At 2 ms (Figure 4a), the dispersed particle front has passed the shock, although considerable particles remain within the fireball and shock-heated air. Because of the initially monodisperse particle size distribution and lack of particle agglomeration model, the particle cloud dispersal is spherical compared to the large-scale jetting observed in the experiment. At 4.0 ms, the particles reside almost entirely within the shock-heated air, where the drag forces cause the particles to lag the primary shock and primarily aerobic particle combustion occurs.
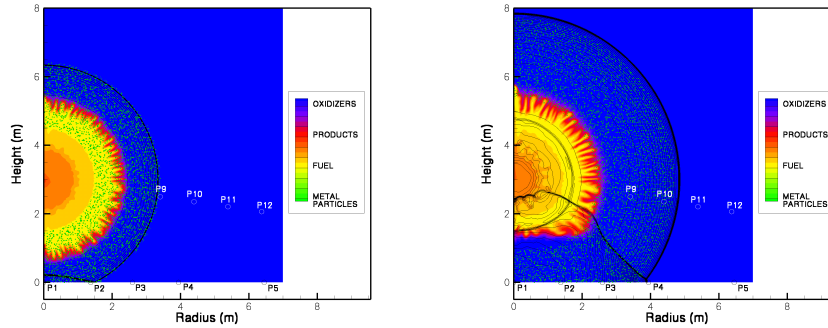
Fig. 4. Composite illustration of HOB chemistry. Spatial distribution of afterburning gas species (fuels) and metal particles including mixing with air oxidizer. Two time instants shown: (a) 2 ms and (b) 4 ms.

5 Metal Particle Afterburning

Metal particle reaction depends on spatial distribution, particle temperature and availability of oxidizing gas species. Figure 5 illustrates the particle concentration relative to the shock system. At this time after the maximum fireball expansion, the particle front lags the incident shock and Mach stem. The highest particle density is concentrated in a layer on the ground, however the gas temperature in this region is less than the particle ignition temperature. Close behind the primary shock, the particle concentration is banded and the particle temperature is above the particle ignition temperature. Afterburning energy release coupled behind the shock was shown by Zarei et al. [6] to provide the optimal blast impulse. This explains why the free-field impulse from IEF is greater than the reference C4, while the situation is reversed at the ground reflection gauges.

The ground reflected shock forms a Mach stem and triple point which pass below the elevated gauge array. Figure 5 illustrates pressure histories at five gauge locations ranging from 3.45 m (gauge P9) to 8.45 m (gauge P14) and shows the primary shock (S_1), ground reflected shock (S_1^R), secondary shock (S_2), reflected secondary shock (S_2^R), and tertiary
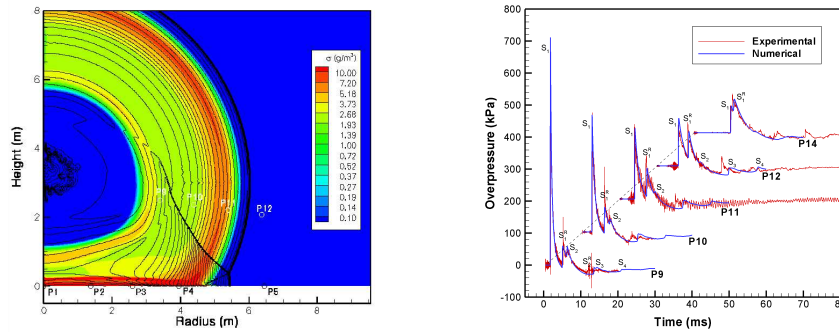
Fig. 5. Particle concentration at 6 ms. Comparison of numerical and experimental results along elevated gauge array.

(S_3) and quaternary (S_4) shocks. Agreement is excellent for all flow features up to the tertiary shock. Tertiary and quaternary shocks are resolved in the numerical results but are noticeably late as compared to experiment. The incident shock arrival time measured using high-speed video against the zebra-board backdrop showed agreement to within ± 0.1 ms for all formulations simulated. Triple-point trajectories were also compared with reasonable results. Peak impulse was compared to experimental results from two orthogonal elevated arrays and far-field ground gauges. Agreement between modeling and experiment is very good. Numerical results are typically within the error band of the experimental results.

6 Heat Release and Energy Partitioning

The small particle size used in the TBX formulations leads to rapid heating to ignition temperature and early-time reaction almost entirely in the detonation products. Reaction of 95% initial metal mass occured after 0.11 ms for TBX1 and 0.81 ms for TBX2. The residual unreacted metal is less than 1% is both TBXs. In contrast, the large granule size in IEF1 has a slower heating time and reaction rate allowing substantial aerobic combustion (42.8%) in the shocked air. Expansion cooling occurs before the IEF particles react completely leaving residual metal amounts of 31.2% IEF1 and 13.1 % in IEF2. Note that the IEFs have much more metal initially.

For IEF1, which contained large granules, the metal particle consumption rate measured using volumetric integration showed that the maximum reaction occurred at about 3 ms, corresponding to substantial aerobic combustion and the triple-point formation time. At 4 ms, particle quenching begins 1 m behind the shock, except in the ground-reflection region where reaction continues until 6 ms. Since the particle reaction occurred within the fireball expansion time (< 4 ms), the energy release timescale contributes to the far-field impulse [3].

Table 1 divides the energy release into detonation energy, gas-phase afterburning, metal reactions with detonation products (anaerobic) and metal reactions with air (aerobic). The TBX formulations showed dominant metal reactions with the detonation products due to the rapid heating time and availability of oxidizing gas species. The metal particles in the IEF1 were slowest to heat, reaching ignition temperature mostly in the

air. The total energy release is related to the triple-point height ranking (see Murray et al. [1]).

The particle size effect and afterburning timescale influence on energy partitioning indicates that a mass scaling (cube-root type scaling) is not appropriate for metalized explosives. This has been more extensively studied by Frost et al. [4] and a multi-energy scaling has further been proposed by Leadbetter et al. [3].

Table 1. Energy Partitioning

Explosive Formulation	Detonation Energy (%)	Gas-Phase Afterburning (%)	Anaerobic Metal Reactions (%)	Aerobic Metal Reactions (%)	Total Energy (MJ/kg)
C4	78.4	21.6	0	0	6.934
TBX1	49.8	19.0	22.4	8.8	8.080
TBX2	34.3	9.8	55.3	0.6	9.567
IEF1	23.3	3.6	18.9	54.2	8.876
IEF2	11.3	7.2	45.8	36.9	12.26

7 Conclusions

Understanding the metalized explosion interaction with a single reflecting surface in the HOB scenario is a prerequisite to interpreting more complex situations involving multiple reflecting surfaces and high confinement. Given that the TBX and IEF explosive classes performed as well or better than the HE reference charge, chemical afterburning of detonation products and metal particle additives contributed substantially to the impulse measured in the near field. Numerical modeling allowed the timescale, degree of reaction and spatial distribution of afterburning components to be studied. Mixing and heating caused by the ground-reflected shock promotes afterburning and dispersal of larger particles into the shock-heated air contributes to near-field impulse and blast pressure.

References

1. Murray S. B., Anderson C. J., Gerrard K. B., Smithson T., Williams K. and Ritzel D.V. Overview of the 2005 Northern Lights Trials, Proc. ISSW26, Gottingen, Germany, 2007
2. Ritzel D. V., Ripley, R. C., Murray S. B., Anderson C. J., Near-Field Blast Phenomenology of Thermobaric Explosions, Proc. ISSW26, Gottingen, Germany, 2007.
3. Leadbetter J., Ripley R. C., Zhang F., Frost D. L., Multiple Energy Scaling of Blast Waves from Heterogeneous Explosives, Proc. 21st ICDERS, Poitiers, France, 2007.
4. Frost D. L., Zhang F., The Nature of Heterogeneous Blast Explosives, Proc. 19th Military Aspects of Blast and Shock, Calgary, Alberta, Canada, 2006.
5. Donahue L., Whitehouse D. R., Josey T., Ritzel D. V., Winter P., Non-Ideal Blast Effects for Vulnerability/Lethality Analysis, Proc. ISB23, Adelaide, Australia, 2004.

6. Zarei Z., Frost D. L., Donahue L., Whitehouse D., Simplified Modeling of Non-Ideal Blast Waves from Metallized Heterogeneous Explosives, Proc. 20th ICDERS, Montreal, Quebec, Canada, 2005.
7. Ripley R. C., Donahue L., Dunbar T. E., Zhang, F., Explosion Performance of Aluminized TNT in a Chamber, Proc. 19th Military Aspects of Blast and Shock, Calgary, Alberta, Canada, 2006.
8. Zhang, F., Yoshinaka, A., Anderson, J., Ripley R. C., Confined Heterogeneous Blast, Proc. 19th Military Aspects of Blast and Shock, Calgary, Alberta, Canada, 2006.